Journal of Alloys and Compounds 509 (2011) 8306–8312

Contents lists available at ScienceDirect

Journal of Alloys and Compounds

journal homepage: www.elsevier.com/locate/jallcom

Structural-controlled synthesis of manganese oxide nanostructures and their electrochemical properties

Yanmin Wang, Haifeng Liu, Mi Bao, Binjia Li, Haifeng Su, Yanxuan Wen, Fan Wang*

School of Chemistry and Chemical Engineering, Guangxi University, Nanning 530004, PR China

ARTICLE INFO

Article history:
Received 14 March 2011
Received in revised form 22 May 2011
Accepted 23 May 2011
Available online 30 May 2011

Keywords:
MnO_2
Oxide materials
Hydrothermal
Electrode materials

ABSTRACT

A structural-controlled synthesis of manganese oxide nanostructures from single Mn_3O_4 precursor via hydrothermal method is presented. The obtained products include α- and β-MnO_2 nanorods, γ-MnO_2 urchin-like microspheres, birnessite nanowires and nanosheets. The morphology evolution process and the effect of varying reaction parameter to the phase and morphology are systematically investigated. The formation mechanisms have been rationalized. The obtained nanostructures are as the model system for studying the electrochemical capacitance performances, which have been investigated by cyclic voltammetry.

1. Introduction

Manganese oxides are of considerable interests because of their high applicability in various fields, like magnetic materials, energy transfer, redox catalysis, and battery materials [1–3]. A class of manganese oxides such as spinel hausmannite Mn_3O_4, birnessite-type MnO_2 and tunnel-based octahedral molecular sieve structures (todorokite, cryptomelane-type α-MnO_2, γ-MnO_2, and pyrolusite β-MnO_2) are possible by interlinking the basic MnO_6 octahedra via edges and vertices [2]. The birnessite-type MnO_2 has a layered structure with a $[2 \times \infty]$ framework, in which metal ions, OH^- ions and water molecules locate in the interlayer space of MnO_6 octahedral layers [4]. The cryptomelane-type α-MnO_2 is constructed from double chains of edge-sharing octahedra, which share corners to form 2×2 tunnel with metal ions in the tunnel. β-MnO_2 is constructed of single chains of edge-sharing octahedra, forming a framework structure with 1×1 tunnels arrays. On the other hand, γ-MnO_2 is considered as a disordered intergrowth of the β-MnO_2 and ramsdellite structures, consisting of a random arrangement of single and double chains of MnO_6 octahedra [5]. The outstanding structural flexibilities of MnO_2 is attractive since it offers a wide alteration of different structure types and provide practically potential systems to research the impact of dimensionality and crystalline structure on catalytic, electrochemical and magnetic properties. Thus, the synthesis approaches of MnO_2 in various morphologies and structures for a very wide variety of applications are of great significance.

Comparing to other soft chemical route in solution, the hydrothermal route is especially adapted to the elaboration of nanostructures since it provides versatile control over crystallization under mild conditions, and act as one of the promising technology due to the low environmental impact and low-cost. Several hydrothermal methods can be used in syntheses of MnO_2 nanostructures as well as other Mn oxides materials such as reduction of MnO_4^-, mixing of MnO_4^- and Mn^{2+}, and oxidation of Mn^{2+} compounds [6–12]. Recently, the synthesis of MnO_2 nanostructures using commercial Mn oxide solid powder, likes MnO_2 and Mn_2O_3, as raw materials by facile hydrothermal treatment has attracted attentions because it not only avoids complicated purification processes but also shows clearly the relationships between phases of the target products and the raw materials [13–18]. Generally, α- [13,14], β- [14], γ-MnO_2 [15–17] and MnOOH [18] nanorods/nanowires were successfully synthesized. In our previous work, we presented a simple surfactant free hydrothermal method to the synthesis of 1D tunnel-based β- and γ-MnO_2 nanostructures using Mn_3O_4 powder as raw materials [19]. In this work, more nanostructure including α-MnO_2 in acid conditions and layered birnessite-type MnO_2 in basic media were obtained. The structures and morphologies of the MnO_2 nanoscale materials can be controlled by adjusting the pH, temperature and additive in the hydrothermal system. This work provides a comprehensive understanding on manganese oxide re-crystallization process, and present phase tuning tools to obtain pure manganese oxide phase with controlled morphologies.

* Corresponding author. Tel.: +86 771 3237022; fax: +86 771 3233718.
E-mail address: fanwang@gxu.edu.cn (F. Wang).

0925-8388/$ – see front matter © 2011 Elsevier B.V. All rights reserved.
doi:10.1016/j.jallcom.2011.05.085

Table 1
Detailed synthetic parameters for the synthesis of Mn oxide nanostructures.

	Mn_3O_4 (mmol)	Solution	Additive reactants (mmol)	Reaction temperature (°C)	Products	Specific surface area ($m^2\ g^{-1}$)
1	3	0.5 M H_2SO_4	–	180	β-MnO_2 nanorods	33
2	3	0.5 M H_2SO_4	–	80	γ-MnO_2 nanourchins	97
3	3	0.5 M H_2SO_4	$K_2Cr_2O_7$ (2.0 mmol)	180	α-MnO_2 nanorods	47
4	0.09	6 M NaOH	–	180	Na-birnessite type nanowires	44
5	0.09	6 M KOH	–	180	K-birnessite type nanosheets	19

2. Experimental

The raw Mn_3O_4 materials were obtained from Qiulong chemical company, Shanghai. All chemicals were of analytical grade and used without further purification. All aqueous solutions were prepared using deionized water. The various manganese oxide nanostructures were synthesized via hydrothermal treatment of Mn_3O_4 powders at different solution for 24 h [19]. To synthesis of α-MnO_2 nanorods, for example, 0.68 g (3 mmol) of Mn_3O_4 powder, 0.8 mL of concentrated H_2SO_4 and 0.6 g (2.0 mmol) of $K_2Cr_2O_7$ were added to 20 mL of deionized water under magnetic stirring, and then the solution was transferred into a 23 mL Teflon-lined autoclave. The autoclave was heated at 180 °C for 24 h. The resulting product was filtered, washed and dried for further characterization. The detail reaction parameters for the preparation are listed in Table 1.

The crystallographic characteristics of the products were characterized by X-ray powder diffraction (XRD) pattern with a Rigaku D/max-2500 X-ray diffractometer equipped with graphite monochromatized high-intensity Cu Kα radiation (λ = 1.54178 Å). The scanning electron microscopy (SEM) images were taken on a Hitachi S-3400N SEM. The nitrogen adsorption–desorption experiments to obtain surface area of the products were performed on a Quantachrome NOVA1000 automated surface area analyzer.

The electrochemical measurement was carried out by cyclic voltammetry on Gamry PCI4/750 electrochemical workstation. The electrode material was a mixture of MnO_2/acetylene black/PVDF with weight ratio of 65/25/10. The mixture and N-methyl pyrrolidone were spread on aluminum foil and further dried at 120 °C for 12 h. The loading level of the active materials was 3 mg/cm^2. The electrochemical cell consisted of a three-electrode system, where the prepared composite materials were used as the working electrode, Pt-sheet as the counter electrode and SCE as the reference electrode. Cyclic voltammetry was carried out at a sweep rate of 5–200 mV s^{-1} over the range 0–1.0 V in 1 M Na_2SO_4 aqueous electrolyte. The specific capacitance C value is calculated as $C(F\,g^{-1}) = Q/(\Delta E \times m)$, where Q is the charge obtained from CV test, ΔE is the voltage window (1.0 V) and m is the mass of the active electrode material.

3. Results and discussion

3.1. Structural and morphological characterization

Fig. 1 shows the XRD spectra of commercial Mn_3O_4 powder and all synthesized MnO_2 products. The XRD pattern of the precursor (Fig. 1a) indicates that the raw material is well crystallized and is composed of hausmannite Mn_3O_4 (JCPDS 80-0382) and MnOOH (65-2776). The patterns of all as-prepared products are significantly different from that of the raw material. As for α-MnO_2, β-MnO_2 and layered birnessite-type MnO_2, the diffraction peaks are sharp and symmetric, indicating that the as-prepared products are well crystallized. The main peaks at 2θ = 22.4, 37.1, 42.1 and 56.1° measured from Fig. 1c can be indexed to the orthorhombic phase of γ-MnO_2, while the observed broad peaks are characteristic of relatively poorly crystallized powder. Therefore, the phases of the Mn oxides products of hydrothermally treated Mn_3O_4 powder are strongly dependent on the synthetic parameters.

The typical shape of Mn_3O_4 precursor and the obtained products were observed by SEM. The raw material has irregular-shaped particles with inhomogeneous size distribution ranging from one to several 10 μm, as shown in Fig. 2a. For as-synthesized products, the β- and α-MnO_2 are characterized by the formation of nanorods (Fig .2b and c). The as-obtained nanorods have uniform diameter around 100 nm with lengths up to 1 μm. Instead, the spherical particles with urchin-like γ-MnO_2 nanostructures are achieved by the assembly of nanorods (Fig. 2d). The particles diameters are about 1–2 μm, while the uniform nanorods have lengths up to about 200 nm and width around 40 nm. The layered Na-birnessite-type (Na-bir) MnO_2 is composed of nanowires with average length over 10 μm and diameter about 100 nm. The uniform nanowires bundles are also observed (Fig. 2e). The K-birnessite-type (K-bir) MnO_2 product only consists of the nanosheets (Fig. 2f). They are usually several or several 10 μm in size and about 20–50 nm in thickness.

N_2 adsorption–desorption studies were performed to determine the surface characteristics. The special surface areas of the obtained Mn oxide nanostructures are listed in Table 1. The results show that the specific surface area is more dependent on the morphologies and nanostructures of prepared MnO_2. The γ-MnO_2 microspheres hold the largest special surface area, suggesting higher electrochemical activity of γ-MnO_2 microspheres.

3.2. Formation mechanism of tunnel-based Mn oxide nanostructures

As demonstrated by the XRD and SEM results, there are obvious differences among the phases and morphologies of the products. The tunnel-typed MnO_2 nanorods are formed in acidic media, while the layered birnessite nanowires are achieved in basic solution. A detailed investigation of the variable transfor-

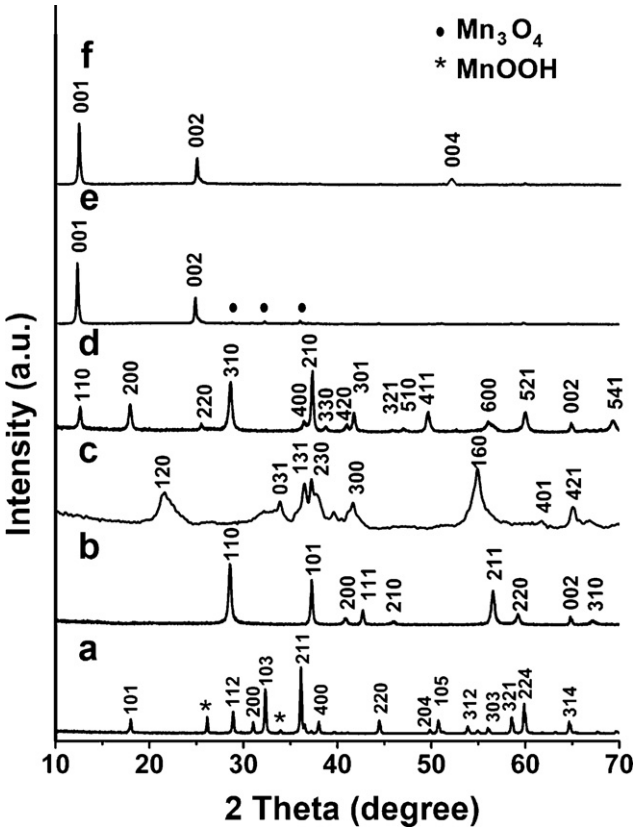

Fig. 1. XRD patterns of (a) commercial Mn_3O_4 powder, (b) β-MnO_2, (c) γ-MnO_2, (d) α-MnO_2, (e) Na-birnessite-type MnO_2 and (f) K-birnessite-type MnO_2.

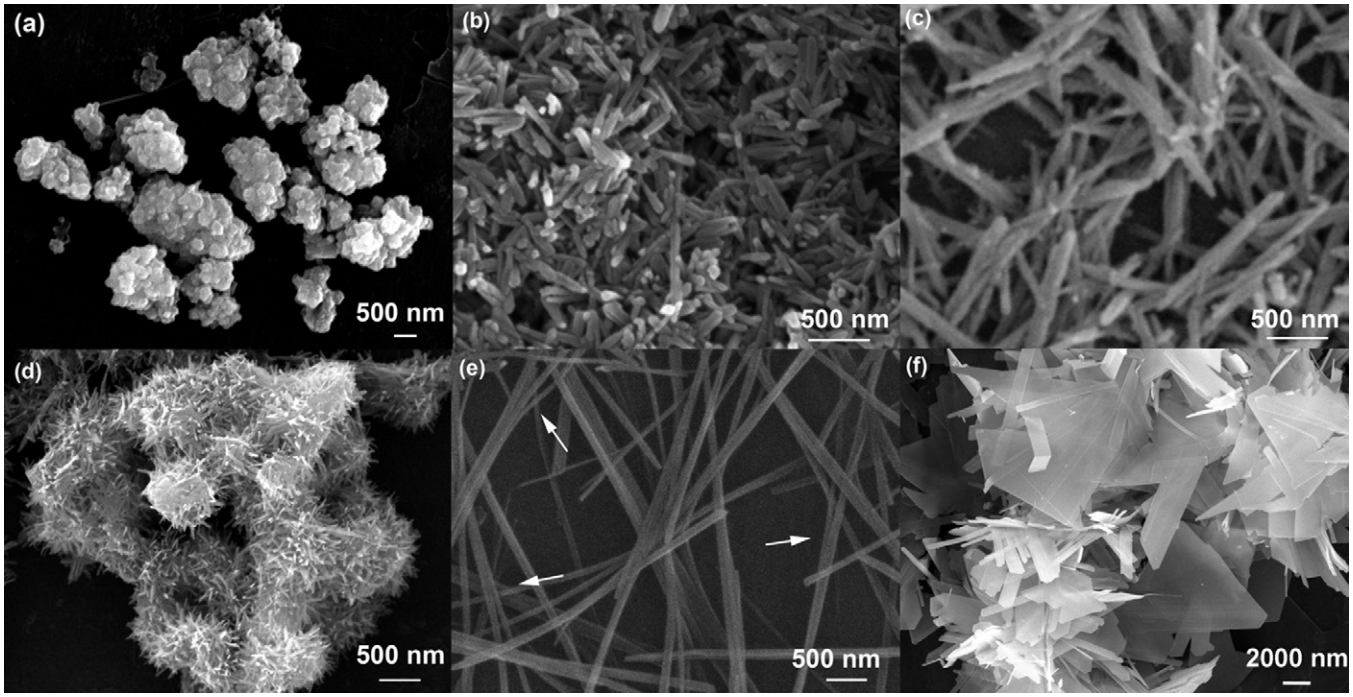

Fig. 2. SEM images of (a) Mn_3O_4 precursor, (b) β-MnO_2 nanorods, (c) α-MnO_2 nanorods, (d) γ-MnO_2 urchin-like nanostructures, (e) Na-bir MnO_2 nanowires and (f) K-bir MnO_2 nanosheets. Arrows in panel e indicate the splitting of nanosheets to nanowires.

mation processes is necessary since it is important to realize the controllable fabrication of nanomaterials with different structures. Up to now, a range of formation mechanism of manganese oxides one-dimension nanostructures, such as rolling growth, self-assembly and dissolution–recrystallization process, has been presented [6,20–22]. In addition, different tunnel-structured manganese oxide may be obtained under different pH conditions via hydrothermal synthesis. In this way, hard cations, like K^+, Mg^{2+} and Rb^+, act as templates to control the size of tunnels since the hydrated cations have various sizes in acidic, neutral and basic conditions [1,9].

Selectively synthesizing various nanostructures of manganese oxide from single precursor provides particularly relevant systems to investigate the impact of phase on physic-chemical properties. In our previous work, the evolutions of phases and morphologies of products were investigated [19]. In acidic solution (pH < 1), Mn_3O_4 tends toward the following fast dismutation reaction:

$$Mn_3O_4 + 4H^+ \rightarrow MnO_2 + 2Mn^{2+} + 2H_2O \quad (1)$$

The transformation of Mn_3O_4 at 80 °C results in the formation of γ-MnO_2 urchin-like nanostructures. However, the metastable γ-MnO_2 will transform into β-MnO_2 oxide with 1 × 1 tunnel structure by hydrothermal treatment at high temperature. γ-MnO_2 acts as the important intermediate at the very beginning of the hydrothermal process, and the symmetrical 1 × 1 tunnel structure of β-MnO_2 acts as directing factor and orients the preferential growth direction of nanorods.

A series of metal sulphates ($NiSO_4$, $CuSO_4$, $MgSO_4$, $(NH_4)_2SO_4$, Na_2SO_4 and K_2SO_4) were introduced into the hydrothermal system to investigate the effect of cations. The XRD patterns of products with the additive cations are shown in Fig. 3a–f. The phases of product still remain β-MnO_2, suggesting that the metal cations have little effect onto the tunnel structure in strong acidic solution.

α-MnO_2 nanostructures are yielded by using $K_2Cr_2O_7$ as oxidant (Fig. 1d). However, the main products by reacting Mn_3O_4 with stronger oxidants ($KClO_3$, $(NH_4)_2S_2O_8$ and $KMnO_4$) in H_2SO_4 solution are β-MnO_2 (Fig. 3g–i). These evidences suggest that the phases of product are also strongly dependent on the kinds of oxidant. By using $KClO_3$, $(NH_4)_2S_2O_8$ and $KMnO_4$ as oxidants, a higher Mn oxidation state (+4) is yielded, which lead to the formation of β-MnO_2 structure. Instead, the lower oxidation states of Mn are achieved by using Cr (VI) oxidant, in which result in the formation of α-MnO_2 phase [22].

To identify the role of Cr compounds that would determine the crystal structure of product, hydrothermal experiments of Mn_3O_4 precursors in different systems containing Cr compounds were carried out. The detailed synthetic conditions are listed in Table 2. For sample b and c, the strong acidic solutions were formed with the soluble CrO_3 acid anhydride. For sample d, the orange–red solution was observed after the reaction due to the oxidation of Cr^{3+} ions into $Cr_2O_7^{2-}$ ions by $KClO_3$. The XRD patterns of the obtained products are shown in Fig. 4. The main forms are of α-MnO_2 phases for those obtained products except the β-MnO_2 phase of the sam-

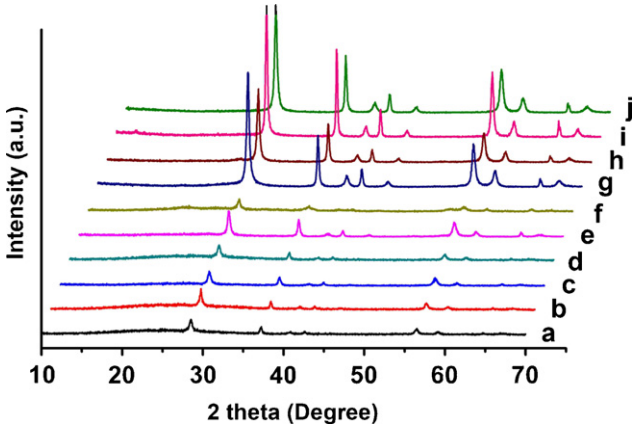

Fig. 3. XRD patterns of the products by reacting Mn_3O_4 with different metal salts and oxidants in H_2SO_4 solution including: (a) $NiSO_4$, (b) $CuSO_4$, (c) $MgSO_4$, (d) $(NH_4)_2SO_4$, (e) Na_2SO_4, (f) K_2SO_4, (g) $KClO_3$, (h) $(NH_4)_2S_2O_8$, (i) $KMnO_4$ and (j) pure β-MnO_2.

Table 2
MnO_2 nanostructures obtained under comparative hydrothermal conditions.

	Mn_3O_4 (mmol)	Additive reactants /mmol	H_2SO_4 (mL)	Color of the solution	Main phase
a	3	K_2SO_4 (2 mmol), CrO_3 (4 mmol)	0.8	Red–orange	α-MnO_2
b	3	K_2SO_4 (2 mmol), CrO_3 (28.8 mmol)	0	Red–orange	α-MnO_2
c	3	CrO_3 (28.8 mmol)	0	Red–orange	α-MnO_2
d	3	$Cr_2(SO_4)_3{\cdot}6H_2O$ (2 mmol), $KClO_3$ (4 mmol)	0.8	Red–orange	α-MnO_2
e	3	$Na_2Cr_2O_7$ (2 mmol)	0.8	Red–orange	α-MnO_2 + ε-MnO_2
f	3	$MgSO_4$ (4 mmol), CrO_3 (28.8 mmol)	0	Red–orange	α-MnO_2 + ε-MnO_2
g	3	$Cr_2(SO_4)_3{\cdot}6H_2O$ (2 mmol)	0.8	Green	β-MnO_2

ple g, which demonstrate that the presence of Cr(VI) ions is greatly important for the formation of α-MnO_2 phase.

The XRD patterns in Fig. 4 also reveal the effects of metal ions. When the reaction is carried out in the absence of K^+, the main form of product is still α-MnO_2 phases (Fig. 4c). A small amount of ε-MnO_2 is found. The morphology of the obtained product is smooth nanorods of about 50 nm diameter and 1–2 μm length (not shown in this article). Similarly, when $Na_2Cr_2O_7$ or $CrO_3 + MgSO_4$ were used as oxidants instead of $K_2Cr_2O_7$, both phases of α-MnO_2 and ε-MnO_2 were obtained simultaneously (Fig. 4e and f). ε-MnO_2 has hexagonal structure with structural faults, which is similar to that of γ-MnO_2. The ε-MnO_2 nanostructures had been synthesized by reacting $MnCl_2$ with $NaClO_4$ [23]. In these studies, the formation of ε-MnO_2 phase should be templated by Na^+ or Mg^{2+} ions since no catalyst or capping agent was used in the hydrothermal process.

3.3. The formation of layered birnessite-type MnO_2 nanowires

Birnessite is a common intermediate for the preparation of tunnel-based octahedral molecular sieve structures. Birnessites containing Na^+, K^+ ions in the interlayer with nanosheets-like morphology is always prepared by redox reactions of MnO_4^- and/or Mn^{2+} or direct conversion of manganese oxides (e.g., Mn_2O_3, Mn_3O_4, etc.) in a basic or dilute acidic medium or by electrochemical conversion from Mn_3O_4 thin films [21,24–27]. In particular, hydrothermal treatment of Mn_2O_3 or Mn_3O_4 powders in NaOH solution leads to the production of Na-bir nanobelts [26], or tunnel structure $Na_{0.44}MnO_2$ nanowires [27]. In our experiment, the morphologies of the obtained materials via hydrothermal treatment of Mn_3O_4 are various in NaOH or KOH solutions. The large sheet-like structures with a few nanowires and the unreacted particles are obtained in 1 M NaOH solution (Fig. 5a). In company with the increase in NaOH concentrations, the Na-bir with nanowires bundle morphology can be synthesized at high yield (Fig. 2e). The morphologies of the obtained materials change to large particles with smooth surfaces in 10 M NaOH solution (Fig. 5b).

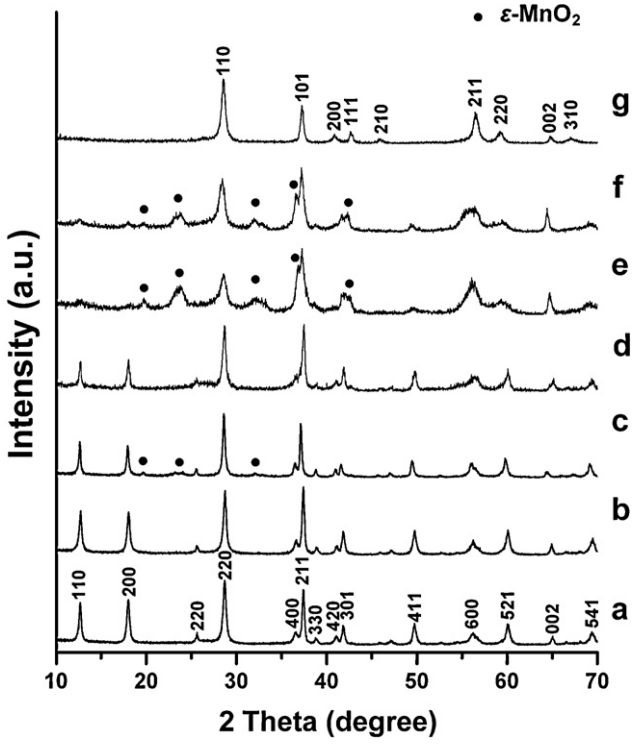

Fig. 4. XRD patterns of MnO_2 samples obtained under different reaction conditions. The detailed reaction condition for each sample (a–g) was listed in Table 2.

Based on the layered structure of birnessite and the experimental results, the splitting process can be proposed to illustrate the formation of Na-bir nanowires [28]. At basic solution, Mn_3O_4 powders are partially converted into birnessite sheet-like structure. Then, the structural reconstruction induced by the migration of some Mn atoms into interlayer positions lead to the splitting of nanosheets to nanowires, as indicated by the arrows in Fig. 2e. The added base in the system determines the formation of nanosheets or nanowires. In high concentrated NaOH solution, birnessite have strong splitting behavior and high solubility under the hydrothermal conditions, resulting in fast growth of the microcrystals.

The effect of the cations is also the key to tune the hydrothermal conversion of Mn_3O_4 in basic solution. In 6 M KOH solution, the products can be recognized as K-bir structure according to the XRD pattern (Fig. 1f). The glittering samples indicate the preparation of anisotropically shaped microcrystals with considerable size. Moreover, most of the nanosheets have angular tips with a specific angle, which may relate to particular crystal planes serving as growth front. Most of the sheets had long and straight edges. This particular morphology is likely occurred from the splitting process. However, the degree of splitting process is more weakened in KOH solution with limited tendency to form nanowires.

A second hydrothermal treatment was adopted to investigate the stability of birnessite nanowires in NaOH solution [27]. The birnessite nanowires were mixed again with 20 mL of 6 M NaOH solution and heated at 180 °C for another 72 h. The XRD profile (Fig. 6a) shows similar but broad diffraction pattern, while the intensities of the main peaks are lower, in which a structural change may take place. However, the product is still composed of nanowires (Fig. 6b). Hence, the broad diffraction peak may be related to the further splitting process in the second hydrothermal treatment. Perceptibly, the increasing transparency of nanowires after second hydrothermal treatment indicates its smaller thickness.

3.4. Electrochemical studies

Electrochemical supercapacitors, which could provide higher power density than conventional electrostatic capacitors, are currently extensively studied. Comparing with other transition-metal

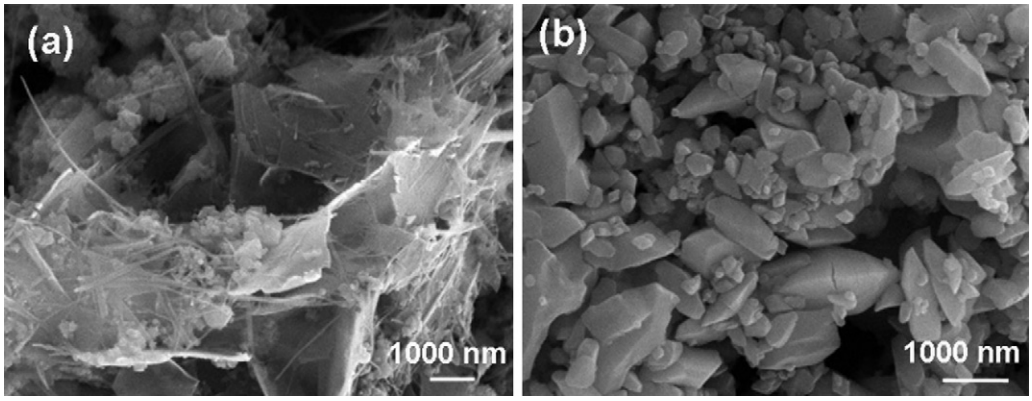

Fig. 5. SEM images of the hydrothermal products synthesized in basic solution at 180 °C for 72 h. (a) 1 M NaOH; (b) 10 M NaOH; (c) 6 M KOH; (d) 10 M KOH.

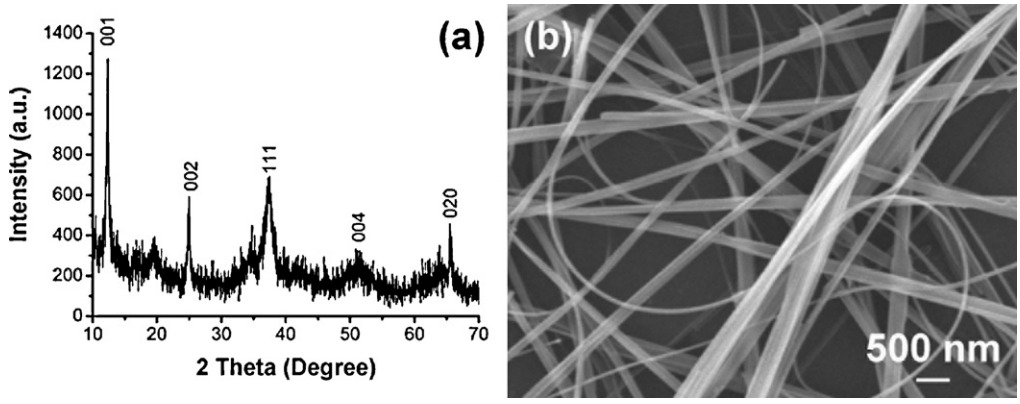

Fig. 6. (a) XRD pattern and (b) SEM image of the Na-birnessite nanowires by a second hydrothermal treatment.

oxide electrode materials, Mn oxides appear to be a promising material with the advantage of low-cost and environmental friendliness and the ability to charge–discharge rapidly [29–33]. The various Mn oxide nanostructures synthesized from single Mn_3O_4 precursors provide a promising system to understand the relationship between the charge-storage characteristics of MnO_2-based electrodes and the corresponding microstructures.

Cyclic voltammetry (CV) curves of the obtained Mn oxides electrodes recorded at 5 mV s^{-1} scan rate are depicted in Fig. 7. The rectangular shapes, in some ways, of α-, β- and γ-MnO_2 nanostructures reveal a pseudo-constant rate of charge–discharge process over the CV cycle. Among all samples, the highest current density is obtained for γ-MnO_2 due to its structural advantages. The 3-D urchin-like microspheres of γ-MnO_2 are composed of finer nanorods, which provide a much larger surface area and the higher porosity. In addition, the γ-MnO_2 polymorph is a highly disordered material, typically having considerable Mn vacancies according to the cation vacancy model proposed by Ruetschi [5]. The vacancies and the corresponding coordination water content provide the kinetically facile sites for the charge transfer and protons/cations diffusion, which also lead to the increase of capacitance. The lowest current density obtained for β-MnO_2 form is due to the narrow 1×1 tunnel, which prevents the insertion of protons and cations. Despite the large 2×2 tunnel size of α-MnO_2, the charge–discharge process may be hindered by the presence of Cr(VI) and K^+ cations inside the tunnel and Na^+ does not have enough space to intercalate into the solid phase, which result in the low CV current density. For comparison, the CV curve of α-MnO_2 nanorods prepared in the absence of K^+ (sample c in Table 2) was measured. The slight increase in current density suggests the restrictive effect of cations inside the tunnel.

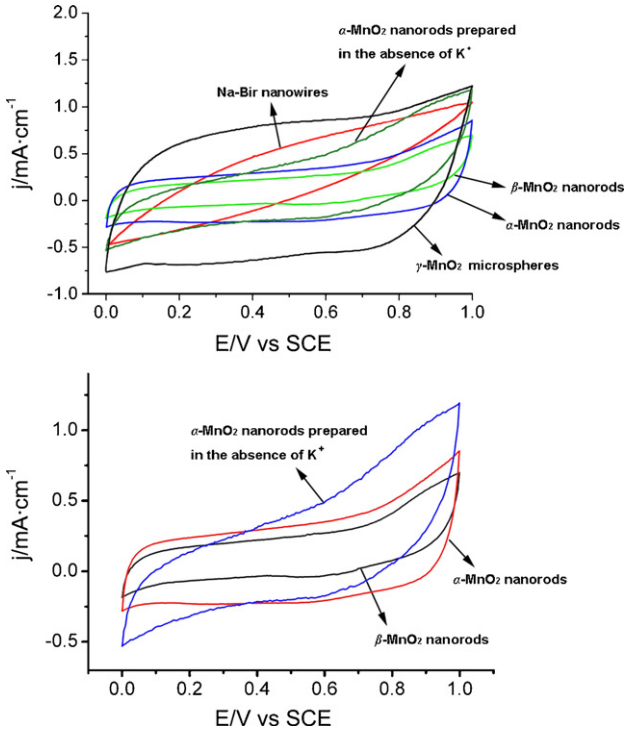

Fig. 7. Cyclic voltammograms of the as-prepared Mn oxide nanostructures and Mn_3O_4 precursor recorded between 0 and 1.0 V vs. SCE in aqueous 1.0 M Na_2SO_4 solution at a scan rate of 5 mV s^{-1}.

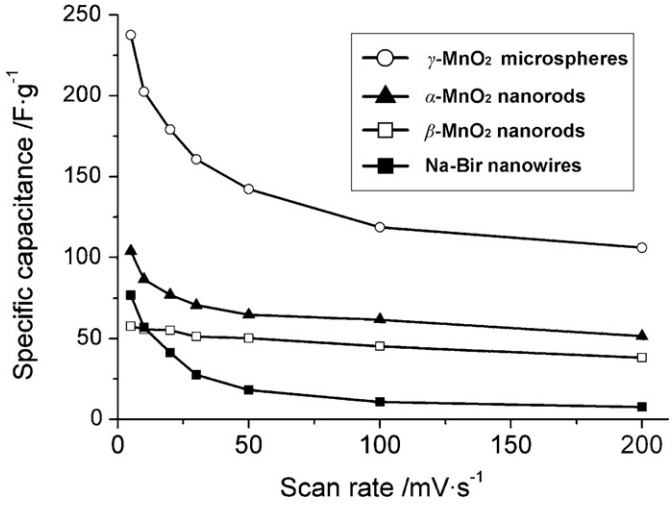

Fig. 8. Relationship between the specific capacitance of the as-prepared Mn oxide nanostructures and Mn_3O_4 precursor and scan rate (5–200 mV s^{-1}).

The rate-dependent CVs of MnO_2 electrodes were investigated over a wide range of scan rates from 5 to 200 mV s^{-1}, as shown in Fig. 8. At 5 mV s^{-1}, the γ-MnO_2 microspheres, α-MnO_2 and β-MnO_2 nanorods possess 237.6, 103.9 and 57.7 F g^{-1} of capacitance, respectively. The *C* value of γ-MnO_2 microsphere reduces to 118.6 F g^{-1} at 100 mV s^{-1} and 105.9 F g^{-1} at 200 mV s^{-1}, with the specific capacitance retentions of 49.9% and 44.6% respectively. The decreasing trend of the capacitance suggests that parts of the surface of the electrode are inaccessible at high charge–discharge rates.

The capacitance values were measured for all as-prepared MnO_2 nanostructure over extended charge–discharge cycling, as shown in Fig. 9. The capacitance values of α- and β-MnO_2 nanorods remain constant during the entire cycling experiments. These results show that no significant modifications on the tunnel structure of α- and β-MnO_2 or corrosion on the electrode are taken place. On the other hand, a significant improvement of the capacitance for γ-MnO_2 is observed. This enhancement in electrochemical performance may be attributed to the gradual change in the microstructures upon cycling.

For Na-bir nanowires, the leaf curve shows an unfavorable capacitive behavior (Fig. 7). The curve also reveals the presence of a large internal resistance even in low scan rate. It is reported that the CV curve of birnessite compound has two redox waves arising from the cations deintercalation and insertion upon redox process [34]. However, the lack of redox waves for Na-birnessite nanowires indicates the exchange limitation of Na^+ ions upon cycling, which result in the low capacitance (76.9 F g^{-1} at 5 mV s^{-1}). This experiment capacitance is greatly lower than that of Na-birnessite compounds reported preciously [32,33]. The Na-birnessite nanowires can sustain a large number of charge/discharge cycles with a capacitance increase (155% after 500 cycles at 30 mV s^{-1}). The increase of *C* values may be due to the activation effect of electrochemical cycling, or mechanical breakdown of the material to expose a higher surface area.

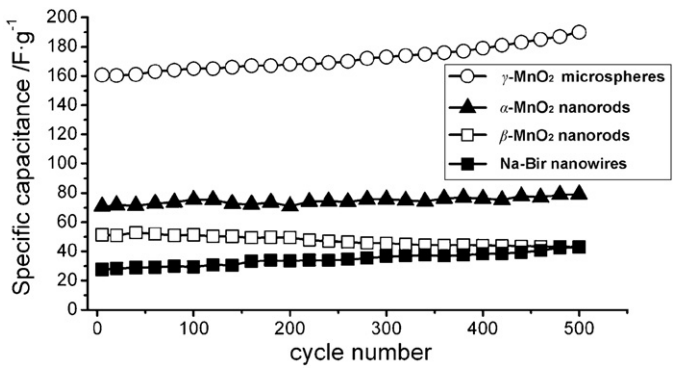

Fig. 9. Capacity retention from Mn oxides electrodes as a function of cycling number (scan rate 30 mV s^{-1}).

4. Conclusion

A hydrothermal synthesis of various Mn oxides nanostructure from single Mn_3O_4 precursor has been reported. This simple route enables pure phase with tuning morphologies to be prepared and the reaction parameters for structural-control are investigated. In acid solution, γ-MnO_2 urchin-like microspheres and β-MnO_2 nanorods were obtained at different reaction temperature, while the α-MnO_2 nanorods were obtained with the addition of Cr(VI) compound. In basic solution, Na-birnessite nanowires and K-birnessite sheets were prepared. The obtained Mn oxide nanostructures were investigated as electrode materials for electrochemical capacitors in 1.0 M Na_2SO_4 aqueous solution. The CV experiments reveal that the crystallographic form as well as the morphology of Mn oxide influences the electrochemical performance. The capacitance values at 5 mV s^{-1} were found to increase in the following order: β-MnO_2 nanorods (57.7 F g^{-1}) < Na-bir nanowires (76.9 F g^{-1}) < α-MnO_2 nanorods (103.9 F g^{-1}) < γ-MnO_2 microspheres (237.6 F g^{-1}).

Acknowledgement

This work was supported by Guangxi Natural Science Foundation (grant no. 0832010)

References

[1] S.L. Suib, J. Mater. Chem. 18 (2008) 1623–1631.
[2] J.E. Post, Proc. Natl. Acad. Sci. U.S.A. 96 (1999) 3447–3454.
[3] S.W. Zhang, G.Z. Chen, Energy Mater. 3 (2008) 186–200.
[4] Z.P. Liu, R.Z. Ma, Y. Ebina, K. Takada, T. Sasaki, Chem. Mater. 19 (2007) 6504–6512.
[5] P. Ruetschi, J. Electrochem. Soc. 131 (1984) 2737–2744.
[6] X. Wang, Y.D. Li, Chem. Eur. J. 9 (2003) 300–306.
[7] Y. Chen, Y.Z. Hong, Y.P. Ma, J.B. Li, J. Alloys Compd. 490 (2010) 331–335.
[8] T. Gao, H. Fjellvåg, P. Norby, Nanotechnology 20 (2009) 055610.
[9] X. Shen, Y. Ding, J. Liu, J. Cai, K. Laubernds, R.P. Zerger, A. Vasiliev, M. Aindow, S.L. Suib, Adv. Mater. 17 (2005) 805–809.
[10] N. Tang, X.K. Tian, C. Yang, Z.B. Pi, Mater. Res. Bull. 44 (2009) 2062–2067.
[11] H.T. Guan, G. Chen, J. Zhu, Y.D. Wang, J. Alloys Compd. 507 (2010) 126–132.
[12] F. Teng, S. Santhanagopalan, Y. Wang, D.D.S. Meng, J. Alloys Compd. 499 (2010) 259–264.
[13] N. Kijima, Y. Sakata, Y. Takahashi, J. Akimoto, T. Kumagai, K. Igarashi, T. Shimizu, Solid State Ionics 180 (2009) 616–620.
[14] M.D. Wei, Y. Konishi, H.S. Zhou, H. Sugihara, H. Arakawa, Nanotechnology 16 (2005) 245–249.
[15] G.Q. Zhang, S.J. Bao, X.G. Zhang, H.L. Li, J. Solid State Electrochem. 9 (2005) 655–659.
[16] Z.Y. Yuan, Z.L. Zhang, G.H. Du, T.Z. Ren, B.L. Su, Chem. Phys. Lett. 378 (2003) 349–353.
[17] G.C. Li, L. Jiang, H.T. Pang, H.R. Peng, Mater. Lett. 61 (2007) 3319–3322.
[18] F. Li, J.F. Wu, Q.H. Qin, Z. Li, X.T. Huang, J. Alloys Compd. 492 (2010) 339–346.
[19] F. Wang, Y.M. Wang, Y.X. Wen, H.F. Su, B. Li, Acta Phys. Chim. Sinica 26 (2010) 521–526.
[20] X. Wang, Y.D. Li, Inorg. Chem. 45 (2006) 7522–7534.
[21] D. Portehault, S. Cassaignon, E. Baudrin, J.P. Jolivet, J. Mater. Chem. 19 (2009) 2407–2416.
[22] I.Y. Kim, H.W. Ha, T.W. Kim, Y. Paik, J.H. Choy, S.J. Hwang, J. Phys. Chem. C 113 (2009) 21274–21282.
[23] Y.S. Ding, X.F. Shen, S. Gomez, H. Luo, M. Aindow, S.L. Suib, Adv. Funct. Mater. 16 (2006) 549–555.
[24] J. Cai, J. Liu, S.L. Suib, Chem. Mater. 14 (2002) 2071–2077.
[25] A.C. Gaillot, B. Lanson, V.A. Drits, Chem. Mater. 17 (2005) 2959–2975.
[26] R.Z. Ma, Y. Bando, L.Q. Zhang, T. Sasaki, Adv. Mater. 16 (2004) 918–922.

[27] Y.G. Li, Y.Y. Wu, Nano Res. 2 (2009) 54–60.
[28] G.C. Li, S.P. Pang, L. Jiang, Z.Y. Guo, Z.K. Zhang, J. Phys. Chem. B 110 (2006) 9383–9386.
[29] D.L. Fang, B.C. Wu, A.Q. Mao, Y. Yan, C.H. Zheng, J. Alloys Comp. 50 (2010) 526–530.
[30] W. Xiao, H. Xia, J.Y.H. Fuh, L. Lu, J. Power Sources 193 (2009) 935–938.
[31] M. Toupin, T. Brousse, D. Belanger, Chem. Mater. 16 (2004) 3184–3190.
[32] S. Devaraj, N. Munichandraiah, J. Phys. Chem. C 112 (2008) 4406–4417.
[33] O. Ghodbane, J.L. Pascal, F. Favier, ACS Appl. Mater. Interfaces 1 (2009) 1130–1139.
[34] L. Athouel, F. Moser, R. Dugas, O. Crosnier, D. Belanger, T. Brousse, J. Phys. Chem. C 112 (2008) 7270–7277.